# Frequency-dependent P-wave anelasticity due to multiscale (fractal) heterogeneities in rocks

Rupeng Ma [a], Jing Ba [a,*], José M. Carcione [a,b]

[a] School of Earth Sciences and Engineering, Hohai University, Nanjing, 211100, China
[b] Istituto Nazionale di Oceanografia e di Geofisica Sperimentale (OGS), Borgo Grotta Gigante 42c, Sgonico, Trieste, 34010, Italy

ARTICLE INFO

ABSTRACT

Understanding the effect that multiscale heterogeneities have on the wave responses of rocks at different frequencies is essential in the interpretation of seismic data. In fact, the behaviors of ultrasonic and seismic waves differ because the experiments involve different spatial scales. Then, a solution is to apply a theory that establishes a relation between the wave properties at different frequency bands considering a size range of heterogeneities. To investigate this problem, we have measured the compressional wave (P-wave) anelasticity (velocity and attenuation) of tight reservoir rocks at ultrasonic, sonic and seismic frequencies. The wave behavior as a function of porosity or clay content shows a consistent trend. With increasing confining pressure, the effect of porosity on attenuation decreases, while that of clay content gradually becomes important. To interpret the data, we propose a double-fractal poroelasticity model by incorporating the self-similarity characteristics of cracks and clay minerals. The comparison between the experimental data and model results reveals the fractality of the clay inclusions and cracks, with radii range of $[10^{-6}, 10^{-1.5}]$ m and $[10^{-6}, 10^{-3.1}]$ m, respectively, which is responsible for the anelastic behavior of the waves on a wide frequency band.

## 1. Introduction

The effects of multi spatial scale (multiscale) pores, cracks and clay minerals on the wave properties, mainly attenuation and velocity dispersion, at different frequency bands, is important for reservoir characterization (to estimate the geofluid content), nuclear-waste disposal analysis, and carbon dioxide flooding and geo-sequestration.[1–4] In this sense, it is essential to perform a comparative analysis between multi-frequency data, namely, seismic (10 Hz-1 kHz), sonic-log (1 kHz–10 kHz) and laboratory (10 Hz-1 MHz) data. Classical poroelasticity theories assuming single-scale heterogeneities are not appropriate. Therefore, we intend to offer data and a model to interpret these data at multiscales and multi-frequencies, in terms of wave anelasticity.

It is well-known that the wave properties are frequency-dependent,[5–13] but only few works analyzed the wave anelasticity data at multi-frequencies. Sams et al.[14] measured attenuation at seismic to ultrasonic frequencies and observed a relaxation peak of the P-wave dissipation factor at sonic frequencies. Caspari et al.[15] estimated the P-wave anelasticity at log and laboratory frequencies, and interpreted the data with the WIFF (wave-induced fluid-flow) model. The problem is that the anelastic properties cannot be scaled from one frequency band

to another, i.e., what we measure at MHz frequencies may not reflect the wave response at seismic frequencies.

The WIFF loss mechanism is widely accepted as a dominant one, which may arise at mesoscopic scales (much smaller than the wavelength but larger than the pore size) when a wave propagates through a fluid-saturated porous medium with heterogeneities.[16–22] The macroscopic WIFF loss mechanism, known as the Biot global flow, is generally important at tens of kHzs,[23,24] while the microscopic WIFF loss mechanism acts at the pore scale, related to stiff pores, grain contacts, cracks and clay aggregates.[25,26] Understanding the WIFF mechanisms, basically the effects on wave anelasticity, can be used to characterize the geometrical properties, mineral composition and fluid content of the rock.[27–37,59,60]

In this work, we carry out P-wave velocity and attenuation measurements at multi-frequencies on tight reservoir rocks of the Ordos Basin, namely, post-stack seismic (at about 30 Hz), well-log (at about 10 kHz) and laboratory (0.55 MHz) data. Then, we analyze the frequency responses and the effects of porosity and clay content on the P-wave anelasticity. To interpret these data sets, we propose a double-fractal poroelasticity model, where fractality refers to the multiple size of the crack radius and clay minerals.

---

* Corresponding author.
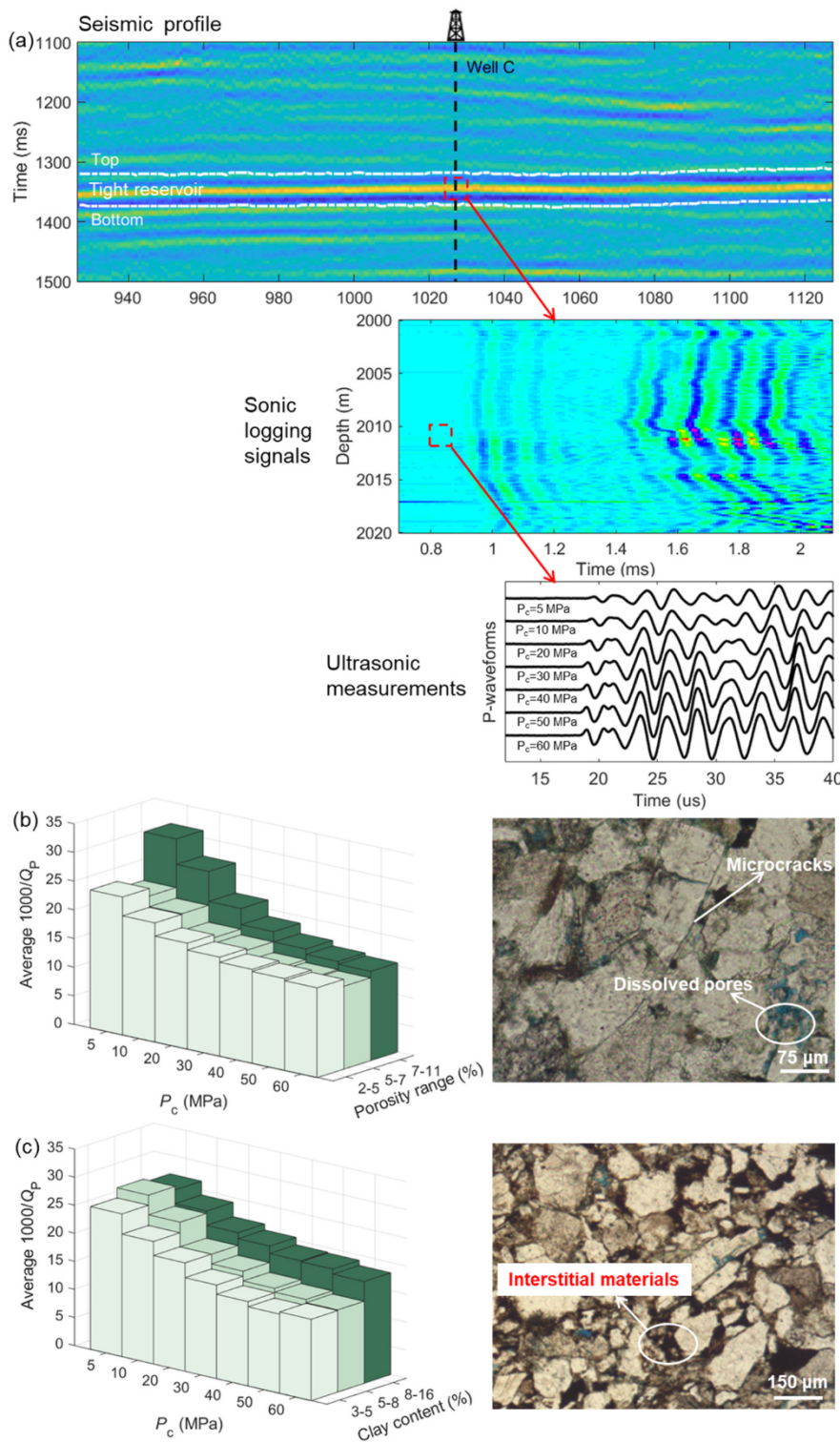  E-mail addresses: jingba@188.com, jba@hhu.edu.cn (J. Ba).

**Fig. 1.** (a) Multi-frequency wave data from a tight reservoir. From top to bottom are shown the seismic profile through Well C, the sonic-log signals from the first receiver in Well C, and the ultrasonic waveforms of specimen TS22 at different confining pressures (Pc). P-wave average attenuation as a function of porosity (b) and clay content (c) at different confining pressures in 38 rock specimens. Casting thin section images are shown, where the upper one exhibits the microcracks and dissolved pores while that lower one has interstitial materials (mostly clay).

## 2. Data acquisition and processing

The Member 7 layer of the Yanchang Formation is located in the Qingyang area of the Ordos Basin, China. The burial depth is between 1840 and 2530 m and the thickness is about 110 m. The in-situ confining and pore pressures are about 30 and 15 MPa, respectively, while the temperature is higher than 30 °C. The reservoir mainly consists of tight sandstones and shales. The sandstone layer has fractures and micro/nano pores. The data are acquired as shown in Fig. 1a.

### 2.1. Laboratory measurements and attenuation estimation

Thirty-eight tight-sandstone samples are collected from the reservoir to perform X-ray diffraction and casting thin section analyses. The minerals are quartz, feldspar, clay minerals, and a small amount of siderite and pyrite, with volume fractions in the ranges of 40–61%, 20–35%, 3–16% and 0.5–3%, respectively. The reservoir space consists of intergranular pores, dissolved pores and microcracks/fractures. The pore diameter lies between 0.02 and 0.05 mm. The interstitial mineral is

**Table 1**
Physical properties of the tight-sandstone specimens.

| Depth (m) | Sample | Density (g/cm³) | Porosity (%) | Permeability (mD) | Clay content (%) |
|---|---|---|---|---|---|
| 1820.5 | TS1 | 2.61 | 2.786 | 0.006 | 5.87 |
| 2009.5 | TS2 | 2.60 | 3.136 | 0.003 | 5.23 |
| 2009.6 | TS3 | 2.61 | 3.467 | 0.004 | 5.92 |
| 2036.5 | TS4 | 2.58 | 3.562 | 0.005 | 6.03 |
| 2000.6 | TS5 | 2.57 | 4.491 | 0.033 | 15.23 |
| 2011.9 | TS6 | 2.57 | 4.512 | 0.007 | 4.08 |
| 2036.7 | TS7 | 2.54 | 4.681 | 0.009 | 4.68 |
| 1995.2 | TS8 | 2.47 | 4.796 | 0.005 | 8.94 |
| 2345.0 | TS9 | 2.57 | 4.819 | 0.017 | 5.85 |
| 1996.7 | TS10 | 2.43 | 5.029 | 0.010 | 4.84 |
| 1996.8 | TS11 | 2.44 | 5.065 | 0.018 | 5.59 |
| 1825.4 | TS12 | 2.57 | 5.192 | 0.021 | 12.31 |
| 1995.4 | TS13 | 2.44 | 5.208 | 0.012 | 6.12 |
| 1992.0 | TS14 | 2.54 | 5.235 | 0.015 | 5.29 |
| 1948.2 | TS15 | 2.53 | 5.278 | 0.005 | 10.96 |
| 2030.0 | TS16 | 2.54 | 5.625 | 0.006 | 5.10 |
| 2030.1 | TS17 | 2.55 | 5.686 | 0.005 | 5.39 |
| 1949.4 | TS18 | 2.51 | 5.787 | 0.020 | 7.84 |
| 1967.0 | TS19 | 2.53 | 6.156 | 0.016 | 5.55 |
| 1819.5 | TS20 | 2.49 | 6.376 | 0.018 | 6.23 |
| 1825.3 | TS21 | 2.49 | 6.917 | 0.013 | 9.39 |
| 2011.8 | TS22 | 2.49 | 7.220 | 0.020 | 5.87 |
| 1825.1 | TS23 | 2.48 | 7.259 | 0.015 | 6.60 |
| 2341.5 | TS24 | 2.48 | 7.327 | 0.019 | 10.96 |
| 1928.9 | TS25 | 2.45 | 7.418 | 0.038 | 5.49 |
| 1929.0 | TS26 | 2.46 | 7.547 | 0.043 | 4.34 |
| 2228.1 | TS27 | 2.47 | 7.674 | 0.074 | 5.19 |
| 1979.6 | TS28 | 2.44 | 7.787 | 0.042 | 4.62 |
| 2098.7 | TS29 | 2.43 | 8.752 | 0.048 | 6.89 |
| 1804.0 | TS30 | 2.43 | 8.791 | 0.056 | 7.16 |
| 1964.0 | TS31 | 2.41 | 8.847 | 0.065 | 7.16 |
| 2121.3 | TS32 | 2.41 | 8.998 | 0.078 | 4.61 |
| 1994.0 | TS33 | 2.42 | 9.000 | 0.036 | 3.46 |
| 2101.8 | TS34 | 2.44 | 9.201 | 0.038 | 7.12 |
| 1800.0 | TS35 | 2.41 | 9.222 | 0.066 | 5.35 |
| 2099.0 | TS36 | 2.41 | 9.252 | 0.072 | 6.22 |
| 2097.7 | TS37 | 2.40 | 9.269 | 0.050 | 5.72 |
| 1996.0 | TS38 | 2.37 | 10.165 | 0.096 | 6.07 |

clay with micropores.

Cylindrical specimens with a diameter of 25.2 mm and lengths in the range 27.30–49.77 mm are cored, and aluminum plugs with the same shape are used as reference standards. The porosity and permeability are measured by the automated permeameter of the Core Measurement System. The rock physical properties of the samples TS1-TS38 numbered according to increasing porosity, are listed in Table 1. Ultrasonic measurements are performed under water saturation and a pulse central frequency of 0.55 MHz. The schematic diagram of the experimental device is illustrated in Ma & Ba.[34] The samples are first saturated with brine by the vacuum-pressure saturation method, then sealed with a rubber sleeve to prevent oil contamination and placed in a high-pressure vessel. Confining pressures of 5 and 10 MPa are applied while keeping a constant pore pressure at 5 MPa and at a temperature of about 30 °C. Furthermore, by keeping the temperature constant, confining pressures of 20, 30, 40, 50 and 60 MPa are applied at a pore pressure of 15 MPa. P-waveforms are recorded after half an hour, and the velocity is computed from first arrivals, with an error less than 0.5%.[38] The spectral-ratio method is used to determine the dissipation factor (inverse of the quality factor $Q$),[39]

$$\ln\left(\frac{A_1(f)}{A_2(f)}\right) = -\frac{\pi x}{Q_P V_P} f + \ln\frac{G_1(x)}{G_2(x)} \quad (1)$$

where $A_1(f)$ and $A_2(f)$ are the amplitude spectra of the rock specimen and aluminium, respectively, $f$ is the frequency, $Q_P$ is the quality factor, $x$ is the propagation distance, $V_P$ is the P-wave velocity, and $G_1(x)/G_2(x)$ is the specimen/aluminium geometrical factor. The attenuation errors can be caused by near-field effects and choice of the time-window

length. Since the near-field region covers a region of 19 mm from the source, which is shorter than the sample length, the related effects do not affect the measurements. Moreover, the window must have a certain length smaller than a given threshold to avoid errors. One period of the waveform after the first arrival is used to compute the amplitude spectrum, avoiding the effect of multiple reflections. The attenuation error can be estimated from the error in fitting a straight line to the spectral ratio data points,[37] which is less than 11%. The centroid frequency-shift method[40] is used to compute the attenuation as well, to verify the results.[30]

### 2.2. Full-waveform sonic-log data and attenuation estimation

Six sets of log data are collected from Wells 1–6, including density log, porosity, gamma ray (GR), velocity and full-waveform signals, recorded at thirteen receivers, with a receiver interval of 0.1524 m and a distance from source to first receiver of 3.12 m. The center frequency of the signals is approximately 10 kHz.

To estimate attenuation from the full-waveform data, the Akaike information criterion (AIC) algorithm is used to obtain the P-wave arrival time.[41] As mentioned above, the attenuation estimated from the sonic-log data is relatively sensitive to the window length among all the processing parameters. A wide window can cause larger errors.[42] We applied a time window of 120 μs after the first arrival to extract the one period of the signal, avoiding the S wave and multiple reflections. Then, the selected pulses are converted into amplitude spectra through the Fourier transform. An example of waveforms and corresponding spectra of the windowed P-waves are given in the "Supplementary Material", respectively. Part of the spectra in the vicinity of the center frequencies is used to compute the attenuation. We use the statistical average method for the subsequent attenuation estimation,[43] as

$$Q_P(z) = \frac{\hat{\Phi}_n(z_0) - \hat{\Phi}_n(z) + Q_P^{-1}(z_0)T_n(z_0)}{T_n(z)} \quad (2)$$

where $\Phi_n = 2\ln A_n(z,f)/f$ and is the matrix associated with depth and frequency, $A_n$ is the spectrum at the $n$th receiver, $T_n$ is the sonic wave travel time, $z$ denotes depth, and the subscript 0 refers to a reference depth. This method suppresses unwanted effects such as receiver mismatch, borehole irregularity, off-centered tool, and weak geometric spreading.

### 2.3. Reservoir properties and seismic attenuation acquisition

The depth interval of the field measurements in the wells is 1770–2200 m, which ensures that these data can be compared with the seismic and laboratory data, the latter made at the in-situ pressure. Thermal effects are not considered because their effect on velocity and waveform in the saturated rocks is negligible at the in-situ conditions.[44] The reservoir lithology includes tight-sandstone and shale rocks. An improved frequency-shift method[45] is used to estimate the attenuation, which removes the effects of the spectrum shape and noise. The attenuation estimated from seismic data can be affected by errors related to the seismic processing (migration, deconvolution, and frequency content), and is locally dependent on the background medium reflectivity.[46] A strong reflection layer above the target layer is selected as the reference. The centroid frequency of the seismic wave is obtained from the spectra with a main frequency range between 0 and 60 Hz.

## 3. Velocity and attenuation

### 3.1. Effects of confining pressure, porosity and clay content

The P-wave velocities and attenuation are given in the Supplementary Material (Figs. S1, S2 and S3). As expected, the ultrasonic P-wave velocity increases and attenuation decreases with confining pressure.
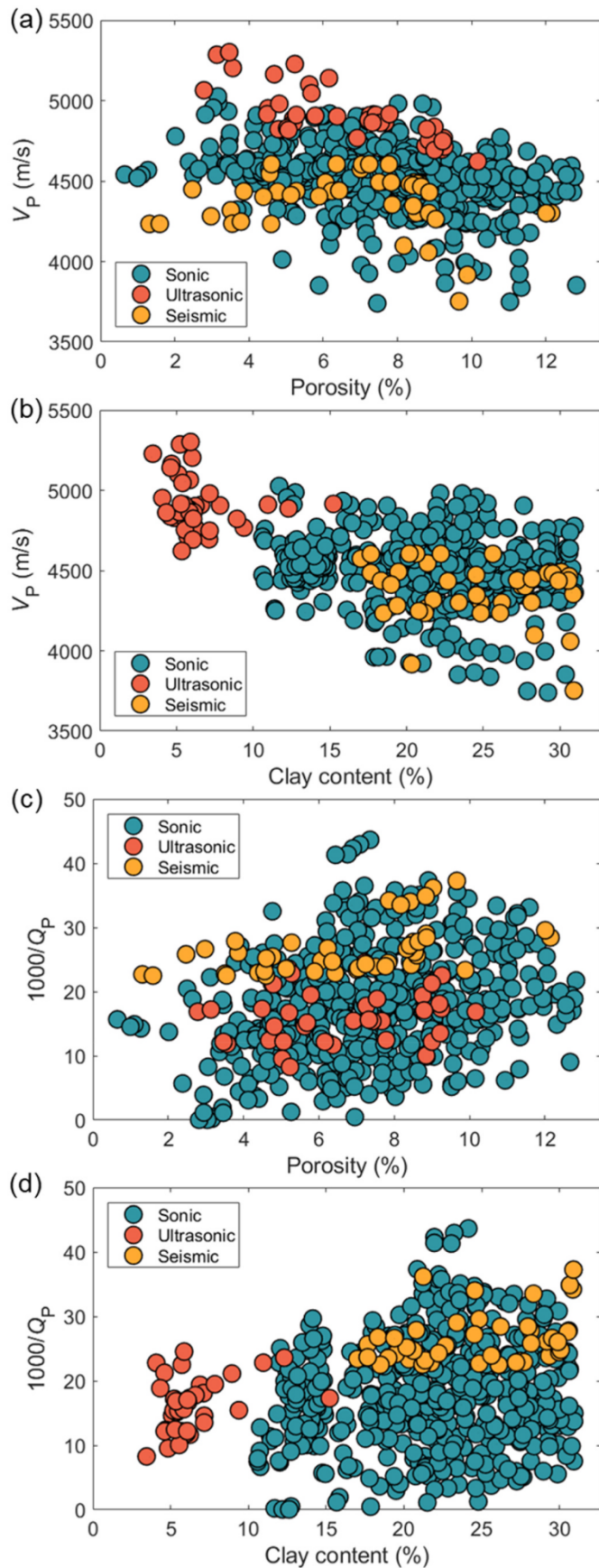
**Fig. 2.** Measured P-wave velocities and attenuation at ultrasonic, sonic, and seismic frequencies. (a) Velocity versus porosity, (b) velocity versus clay content, (c) attenuation versus porosity, and (d) attenuation versus clay content.

The specimens with a higher porosity undergo larger variations.

The 38 specimens are classified into three groups according to porosity and clay content. The averages of attenuation at different ranges of porosity (2–5%, 5–7%, and 7–11%) and clay content (3–5%, 5–8%, and 8–16%) are shown in Fig. 1b and c, respectively. The variation of the P-wave attenuation in different porosity ranges (it generally increases with increasing porosity) diminishes with increasing pressure due to the gradual closing of cracks. On the other hand, the variation with respect to clay content becomes important with increasing pressure. When cracks (associated with the connected pores) gradually close, the crack-associated WIFF loss mechanism is inhibited. On the other hand, intrapore and grain surface clays are hardly affected by pressure, since this clay is not load bearing. The clay-associated WIFF gradually becomes dominant.

### 3.2. Comparison of multi-frequency data

The confining and pore pressures of the reservoir are approximately 30 and 15 MPa, respectively. Fig. 2 compares the P-wave ultrasonic, sonic and seismic velocity and attenuation as a function of porosity or clay content. Generally, the velocity decreases with porosity and clay content while attenuation increases. The wave anelasticity is affected by the combined effects of the pore structure and clay minerals.

A strong velocity dispersion is observed. The ultrasonic velocity has an average of 4912 m/s, compared to 4503 and 4376 m/s at sonic and seismic frequencies, respectively. The average ultrasonic, sonic and seismic dissipation factors ($1000/Q_P$) are 16.22, 18.32 and 26.53, respectively, i.e., the seismic attenuation is higher than the ultrasonic one at constant porosity. The variation range of the sonic attenuation is larger than those at ultrasonic and seismic frequencies.

## 4. Theoretical modeling

### 4.1. Fractal cracks and clay minerals

The shallow crust and particularly fluid-saturated reservoirs contain cracks of different spatial scales, and the presence of clay minerals with micropores can significantly affect the fabric structures. This complexity can be quantitatively described by a fractal geometry, which may be evaluated from Scanning Electron Microscope (SEM) tests.[47–49] We assume that fluid-saturated cracks and clay minerals are both randomly and sparsely distributed in an isotropic medium, satisfying a statistical self-similarity at different scales as shown in Fig. 3. The probability density function of the crack or clay mineral radius distribution is,[50]

$$f(a) = D_f a_{\min}^{D_f} a^{-(D_f+1)} \tag{3}$$

where $a$ and $a_{\min}$ are the random and minimum crack or clay mineral radii, respectively, and $D_f$ is the fractal dimension ranging from 1 to 2 (2D space) and from 2 to 3 (3D space).

### 4.2. Double-fractal poroelasticity model

The clay aggregates with a scale range from microns to meters constitute matrix heterogeneities (Fig. 3). Moreover, the sizes of cracks and grain contacts (soft pores) are in the similar spatial range. The host medium, with an absolute porosity $\varphi$, is composed of the main minerals and stiff pores. The volume fraction of crack inclusions with radius $a_{cr}$ and porosity $\varphi_{cr}$ is $v_{cr}$. The volume fraction of clay inclusion with the radius $a_{cl}$ and porosity $\varphi_{cl}$ is $v_{cl}$. Then, the crack or clay inclusions with different volume fractions ($d\varphi_{cr} = \varphi_{cr} dv_{cr}$ or $d\varphi_{cl} = \varphi_{cl} dv_{cl}$, where the subscript cr or cl denotes crack or clay) are incrementally added to the host by assuming a dilute concentration. The composite obtained after each addition is taken as the host of the next addition. The dry-rock moduli are determined by the following differential scheme,[51]
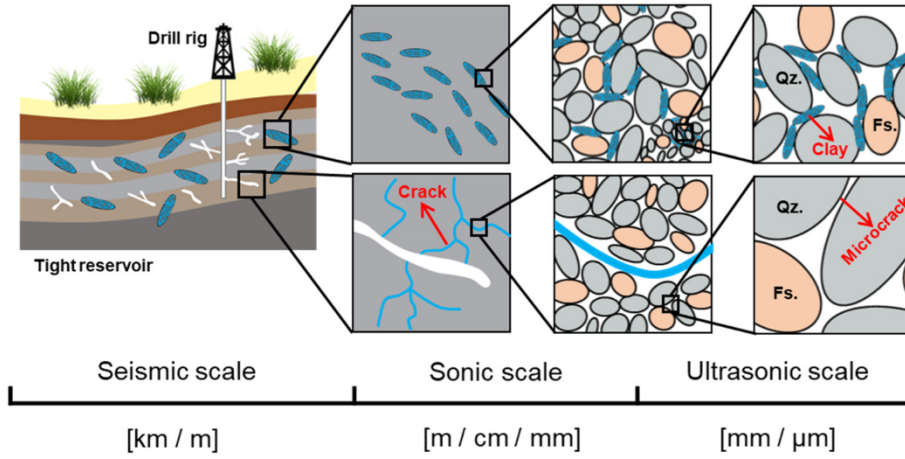
**Fig. 3.** Diagrams showing the double-fractal characterization with cracks and clay inclusions. Qz. is quartz, and Fs. is feldspar.

$$dK_b(v_{cr}) = \frac{(K_{bcr} - K_b)L_1(v_{cr})}{1 - v_{cr}} dv_{cr} \tag{4}$$

$$dK_b(v_{cl}) = \frac{(K_{bcl} - K_b)L_1(v_{cl})}{1 - v_{cl}} dv_{cl} \tag{5}$$

$$dG_b(v_{cr}) = \frac{(G_{bcr} - G_b)L_2(v_{cr})}{1 - v_{cr}} dv_{cr} \tag{6}$$

$$dG_b(v_{cl}) = \frac{(G_{bcl} - G_b)L_2(v_{cl})}{1 - v_{cl}} dv_{cl} \tag{7}$$

where $K_b(v_{cr} = 0, v_{cl} = 0) = K_{bH}$, and $G_b(v_{cr} = 0, v_{cl} = 0) = G_{bH}$. $K_{bH}$ and $G_{bH}$, $K_{bcr}$ and $G_{bcr}$, and $K_{bcl}$ and $G_{bcl}$ are the dry-rock bulk and shear moduli of the host, crack inclusion and clay inclusion, respectively, and $L_1$ and $L_2$ are the polarization factors for the bulk and shear moduli, respectively.

At each addition with a different scale inclusion, the double-porosity model[52,53] with the host porosity $\varphi$ and the incremental porosity $d\varphi_{cr}$ or $d\varphi_{cl}$, ($d\varphi_{cr} = \varphi'_{cr}(a_{cr})da_{cr}$ or $d\varphi_{cl} = \varphi'_{cl}(a_{cl})da_{cl}$), is applied to compute the complex moduli of the composite. Then, the double-fractal equations for wave propagation are

$$\overline{N}\nabla^2\mathbf{u} + (\overline{A} + \overline{N})\nabla e + \overline{Q}_H \varphi \nabla \left( \xi_H + \int_0^\infty \zeta_{cr}\varphi'_{cr}(a_{cr})da_{cr} + \int_0^\infty \zeta_{cl}\varphi'_{cl}(a_{cl})da_{cl} \right)$$
$$+ \int_0^\infty \overline{Q}_{cr}\varphi'_{cr}(a_{cr})\nabla(\xi_{cr} - \varphi\zeta_{cr})da_{cr} + \int_0^\infty \overline{Q}_{cl}\varphi'_{cl}(a_{cl})\nabla(\xi_{cl} - \varphi\zeta_{cl})da_{cl}$$
$$= \overline{\rho}_{00}\ddot{\mathbf{u}} + \overline{\rho}_{01}\varphi\ddot{\mathbf{U}}_H + \int_0^\infty \overline{\rho}_{02}\varphi'_{cr}(a_{cr})\ddot{\mathbf{U}}_{cr}da_{cr} + \int_0^\infty \overline{\rho}_{03}\varphi'_{cl}(a_{cl})\ddot{\mathbf{U}}_{cl}da_{cl}$$
$$+ \frac{\varphi\overline{\varphi}_H \eta}{\overline{\kappa}_H}(\dot{\mathbf{u}} - \dot{\mathbf{U}}_H) + \eta \int_0^\infty \frac{\varphi_{cr}}{\kappa_{cr}}(\dot{\mathbf{u}} - \dot{\mathbf{U}}_{cr})\varphi'_{cr}(a_{cr})da_{cr} + \eta \int_0^\infty \frac{\varphi_{cl}}{\kappa_{cl}}(\dot{\mathbf{u}} - \dot{\mathbf{U}}_{cl})\varphi'_{cl}(a_{cl})da_{cl} \tag{8a}$$

$$\overline{Q}_H\nabla e + \overline{R}_H\nabla\left( \xi_H + \int_0^\infty \varphi'_{cr}(a_{cr})\zeta_{cr}da_{cr} + \int_0^\infty \varphi'_{cl}(a_{cl})\zeta_{cl}da_{cl} \right)$$
$$= \overline{\rho}_{01}\ddot{\mathbf{u}} + \overline{\rho}_{11}\ddot{\mathbf{U}}_H - \frac{\overline{\varphi}_H \eta}{\overline{\kappa}_H}(\dot{\mathbf{u}} - \dot{\mathbf{U}}_H) \tag{8b}$$

$$\overline{Q}_{cr}\nabla e + \overline{R}_{cr}\nabla(\xi_{cr} - \varphi\zeta_{cr}) + \overline{Q}_{cl}\nabla e + \overline{R}_{cl}\nabla(\xi_{cl} - \varphi\zeta_{cl})$$
$$= \overline{\rho}_{02}\ddot{\mathbf{u}} + \overline{\rho}_{03}\ddot{\mathbf{u}} + \overline{\rho}_{22}\ddot{\mathbf{U}}_{cr} + \overline{\rho}_{33}\ddot{\mathbf{U}}_{cl} - \frac{\varphi_{cr}}{\kappa_{cr}}(\dot{\mathbf{u}} - \dot{\mathbf{U}}_{cr}) - \frac{\varphi_{cl}}{\kappa_{cl}}(\dot{\mathbf{u}} - \dot{\mathbf{U}}_{cl}) \tag{8c}$$

$$\left( \overline{Q}_H e + \overline{R}_H \left( \xi_H + \int_0^\infty \zeta_{cr}\varphi'_{cr}(a_{cr})da_{cr} + \int_0^\infty \zeta_{cl}\varphi'_{cl}(a_{cl})da_{cl} \right) \right)$$
$$- (\overline{Q}_{cr}e + \overline{R}_{cr}(\xi_{cr} - \varphi\zeta_{cr})) - (\overline{Q}_{cl}e + \overline{R}_{cl}(\xi_{cl} - \varphi\zeta_{cl}))$$
$$= \frac{1}{3}a_{cr}^2\varphi\varphi_{cr}\left( \frac{\rho_f}{\overline{\varphi}_H}\ddot{\zeta} + \frac{\eta}{\overline{\kappa}_H}\dot{\zeta}_{cr} \right) + \frac{1}{3}a_{cl}^2\varphi\varphi_{cl}\left( \frac{\rho_f}{\overline{\varphi}_H}\ddot{\zeta}_{cl} + \frac{\eta}{\overline{\kappa}_H}\dot{\zeta}_{cl} \right) \tag{8d}$$

where $\mathbf{u}$, $\mathbf{U}_H$, $\mathbf{U}_{cr}$ and $\mathbf{U}_{cl}$ are the solid displacement, fluid displacement in the host medium, fluid displacement in the crack inclusions, and fluid displacement in the clay inclusions, respectively, and $e$, $\xi_H$, $\xi_{cr}$ and $\xi_{cl}$ are the corresponding displacement divergence fields. Scalar $\zeta_{cr}$ ($\zeta_{cl}$) represents the variation of fluid content between the host and cracks (clay aggregates), $\kappa_H$, $\kappa_{cr}$ and $\kappa_{cl}$ are the permeabilities of the host, crack and clay inclusions, respectively, and $\rho_f$ and $\eta$ are the fluid density and viscosity. The host parameters $\overline{\varphi}_H$ and $\overline{\kappa}_H$, the stiffnesses $\overline{A}$, $\overline{N}$, $\overline{Q}_H$, $\overline{Q}_{cr}$, $\overline{Q}_{cl}$, $\overline{R}_H$, $\overline{R}_{cr}$, and $\overline{R}_{cl}$, and the density coefficients $\overline{\rho}_{00}, \overline{\rho}_{01}, \overline{\rho}_{02}, \overline{\rho}_{03}, \overline{\rho}_{11}, \overline{\rho}_{22}$ and $\overline{\rho}_{33}$ can be determined as the discretization procedure illustrated in Zhang et al.[53] The P- and S-wave complex wave numbers ($k_P$ and $k_S$) are obtained by a plane wave analysis.

The P-wave phase velocity is[16,29]

$$V_P = \frac{\omega}{\text{Re}(k_P)} \tag{9}$$

and the dissipation factor is

$$Q^{-1} = \frac{2\text{Im}(k_P)}{\text{Re}(k_P)} \tag{10}$$

*4.3. Data interpretation*

We use the proposed double-fractal model to interpret the multi-frequency experimental data. The grain bulk modulus is 38.78 GPa, based on the Hashin-Shtrikman bounds[54] by assuming quartz as the host mineral; its density is 2.65 g/cm³. The bulk/shear moduli of the dry host medium are 26/19 GPa, 22/17 GPa, and 18/14 GPa at the porosities of 4%, 8% and 12%, respectively. The bulk modulus, density and viscosity of the saturating fluid at the in-situ conditions are 2.273 GPa, 1.004 g/cm³ and 981 Pa·s, respectively.[55] Crack inclusions with a bulk modulus of 0.3 GPa, a shear modulus of 0.21 GPa and a porosity of 0.09 are assumed, while the clay inclusions have a bulk modulus of 0.5 GPa, a shear modulus of 0.17 GPa and a porosity of 0.02.[29] The crack and clay volume fractions for each radius are determined with the probability density function Eq. (3). Uncertainties of the fractal dimension and radius range slightly affect the predicted velocity and attenuation. A higher fractal dimension may lead to a slightly lower P-wave velocity and a broader frequency range of anelasticity. A fractal dimension of 2.58 for the crack is chosen, based on the analysis of pore throats of tight sandstones in the Ordos Basin.[56] The clay inclusions have a fractal dimension of 2.43, based on the properties of clay minerals observed on 2D SEM images.[57] The radius ranges are $[10^{-6}$ m, $10^{-3.1}$ m] and $[10^{-6}$ m, $10^{-1.5}$ m] for cracks and clay, respectively, which are determined by matching the model with the multi-frequency data.

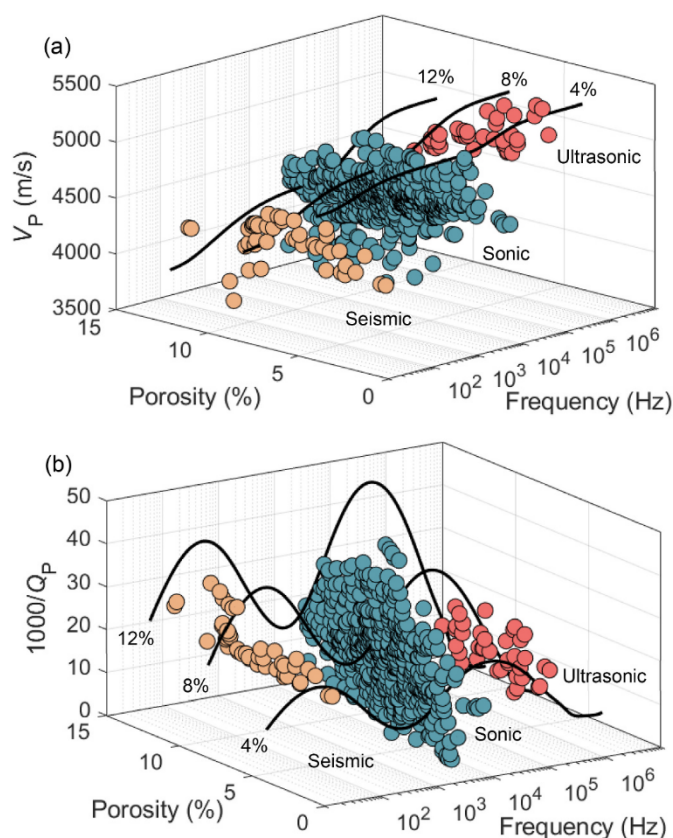The multi-frequency data, compared with the model results at

**Fig. 4.** Predictions of the double-fractal model as a function of porosity and frequency, compared with the experimental data. (a) Velocity and (b) dissipation factor.

different porosities, are shown in Fig. 4. The predictions are in agreement with the observed velocities and attenuation. For instance, the deviations between the theoretical velocity and attenuation and those experimental data of sample TS17 are 1.1% and 6.7%, respectively. There are two attenuation peaks caused by the double-fractal clay and crack inclusions. The attenuation at the seismic band is mostly related to the WIFF mechanism between the clay inclusions and host medium, while the sonic and ultrasonic attenuation are caused by the WIFF due to the cracks and clay inclusions. Other WIFF models can only make predictions at a single frequency band, such as the squirt-flow model.[58] The proposed model offers new approaches for the seismic exploration of reservoirs. By using a multiscale geophysical data set, the elastic properties and attenuation acquired at different frequencies can be related to the crack and inclusions (e.g., clay) properties, leading to effective properties. This is of importance for rock characterization based on laboratory and well data for inferring petrophysical properties from seismic data.

## 5. Conclusions

We have measured the P-wave velocity and attenuation of tight reservoir rocks at different frequency bands. The results show that the effect of porosity on attenuation decreases when that of clay content increases with confining pressure at the ultrasonic scale. In general, the effect of porosity and clay minerals have a similar effect at the different bands. To interpret the data, we propose a double-fractal poroelasticity model, where fractality refers to the size of the cracks and clay inclusions. The agreement between the predictions and the observed data indicates that the P-wave anelasticity can be interpreted by multiscale wave-induced fluid flow (WIFF) mechanisms caused by cracks and clay inclusions with fractal dimensions of 2.58 and 2.43, and radii in the

range $[10^{-6}$ m, $10^{-3.1}$ m$]$ and $[10^{-6}$ m, $10^{-1.5}$ m$]$, respectively. The proposed model also provides an effective tool to correlate data at different frequency bands, which is relevant for the characterization of petrophysical properties.

The proposed model can be applied to fluid-saturated media, but cannot deal with partial saturation at the pore-scale level, e.g., including effects such as capillary forces between immiscible fluids, a topic that will be tackled in a future publication.

## Declaration of competing interest

The authors declare that they have no known competing financial interests or personal relationships that could have appeared to influence the work reported in this paper.

## Data availability

I have shared the link to my data at the Attach File step.

## Appendix A. Supplementary data

Supplementary data to this article can be found online at https://doi.org/10.1016/j.ijrmms.2022.105297.

## References

1 Bailly C, Fortin J, Adelinet M, Hamon Y. Upscaling of elastic properties in carbonates: a modeling approach based on a multiscale geophysical data set. *J Geophys Res Solid Earth*. 2019;124(12):13021–13038. https://doi.org/10.1029/2019JB018391.
2 Chitale V, Alabi G, Gramin P, Lepley SW, Piccoli L. Reservoir characterization challenges due to the multiscale spatial heterogeneity in the presalt carbonate sag formation, North Campos Basin, Brazil. *Petrophysics*. 2015;56:552–576, 06.
3 Radwan AE, Trippetta F, Kassem AA, Kania M. Multi-scale characterization of unconventional tight carbonate reservoir: insights from October oil filed, Gulf of Suez rift basin, Egypt. *J Pet Sci Eng*. 2021;197, 107968. https://doi.org/10.1016/j.petrol.2020.107968.
4 Wang J, Zhang Y, Xie J. Influencing factors and application prospects of CO2 flooding in heterogeneous glutenite reservoirs. *Sci Rep*. 2020;10:1839. https://doi.org/10.1038/s41598-020-58792-z.
5 Carcione JM, Gurevich B, Santos JE, Picotti S. Angular and frequency-dependent wave velocity and attenuation in fractured porous media. *Pure Appl Geophys*. 2013;170(11):1673–1683. https://doi.org/10.1007/s00024-012-0636-8.
6 Caspari E, Milani M, Rubino JG, Müller TM, Quintal B, Holliger K. Numerical upscaling of frequency-dependent P- and S-wave moduli in fractured porous media. *Geophys Prospect*. 2016;64(4):1166–1179. https://doi.org/10.1111/1365-2478.12393.
7 David EC, Fortin J, Schubnel A, Guéguen Y, Zimmerman RW. Laboratory measurements of low- and high-frequency elastic moduli in Fontainebleau sandstone. *Geophysics*. 2013;78(5):D369–D379. https://doi.org/10.1190/geo2013-0070.1.
8 Pang S, Stovas A, Xing H. Frequency-dependent anisotropy in partially saturated porous rock with multiple sets of meso-scale fractures. *Geophys J Int*. 2021;227. https://doi.org/10.1093/gji/ggab204.
9 Subramaniyan S, Quintal B, Madonna C, Saenger EH. Laboratory-based seismic attenuation in Fontainebleau sandstone: evidence of squirt flow. *J Geophys Res Solid Earth*. 2015;120(11):7526–7535. https://doi.org/10.1002/2015JB012290.
10 Vinci C, Renner J, Steeb H. On attenuation of seismic waves associated with flow in fractures. *Geophys Res Lett*. 2014;41(21):7515–7523. https://doi.org/10.1002/2014GL061634.
11 Xu M, Yin X, Zong Z. Wave dispersion and attenuation due to multi-scale wave-induced fluid flow in layered partially saturated pore-crack media. *J Pet Sci Eng*. 2022;208, 109447. https://doi.org/10.1016/j.petrol.2021.109447.
12 Yang H, Duan HF, Zhu JB. Ultrasonic P-wave propagation through water-filled rock joint: an experimental investigation. *J Appl Geophys*. 2019;169:1–14. https://doi.org/10.1016/j.jappgeo.2019.06.014.
13 Yang H, Duan HF, Zhu J. Effects of filling fluid type and composition and joint orientation on acoustic wave propagation across individual fluid-filled rock joints. *Int J Rock Mech Min Sci*. 2020;128, 104248. https://doi.org/10.1016/j.ijrmms.2020.104248.

14  Sams MS, Neep JP, Worthington MH, King MS. The measurement of velocity dispersion and frequency-dependent intrinsic attenuation in sedimentary rocks. *Geophysics*. 1997;62(5):1456–1464. https://doi.org/10.1190/1.1444249.

15  Caspari E, Qi Q, Lopes S, et al. Wave attenuation in partially saturated porous rocks — new observations and interpretations across scales. *Lead Edge*. 2014;33(6):606–614. https://doi.org/10.1190/tle33060606.1.

16  Carcione JM. *Wave Fields in Real Media: Wave Propagation in Anisotropic, Anelastic Porous and Electromagnetic Media*. fourth ed. Elsevier Science; 2022.

17  Carcione JM, Morency C, Santos JE. Computational poroelasticity — a review. *Geophysics*. 2010;75(5):75A229–75A243. https://doi.org/10.1190/1.3474602.

18  Dvorkin J, Mavko G, Nur A. Squirt flow in fully saturated rocks. *Geophysics*. 1995;60(1):97–107. https://doi.org/10.1190/1.1443767.

19  Müller TM, Gurevich B, Lebedev M. Seismic wave attenuation and dispersion resulting from wave-induced flow in porous rocks — a review. *Geophysics*. 2010;75(5):147–164. https://doi.org/10.1190/1.3463417.

20  Müller TM, Gurevich B. Wave-induced fluid flow in random porous media: attenuation and dispersion of elastic waves. *J Acoust Soc Am*. 2005;117(5):2732–2741. https://doi.org/10.1121/1.1894792.

21  O'Connell RJ, Budiansky B. Viscoelastic properties of fluid-saturated cracked solids. *J Geophys Res*. 1977;82(36):5719–5735. https://doi.org/10.1029/JB082i036p05719.

22  Zhao L, Han D hua, Yao Q, Zhou R, Yan F. Seismic reflection dispersion due to wave-induced fluid flow in heterogeneous reservoir rocks. *Geophysics*. 2015;80(3):D221–D235. https://doi.org/10.1190/geo2014-0307.1.

23  Biot MA. Theory of propagation of elastic waves in a fluid-saturated porous solid. I. Low-frequency range. *J Acoust Soc Am*. 1956;28(2):168–178. https://doi.org/10.1121/1.1908239.

24  Biot MA. Theory of propagation of elastic waves in a fluid-saturated porous solid. II. Higher frequency range. *J Acoust Soc Am*. 1956;28(2):179–191. https://doi.org/10.1121/1.1908241.

25  Best AI. The effect of pressure on ultrasonic velocity and attenuation in near-surface sedimentary rocks. *Geophys Prospect*. 1997;45(2):345–364. https://doi.org/10.1046/j.1365-2478.1997.00344.x.

26  Mavko G, Jizba D. Estimating grain-scale fluid effects on velocity dispersion in rocks. *Geophysics*. 1991;56(12):1940–1949. https://doi.org/10.1190/1.1443005.

27  Adam L, Batzle M, Lewallen KT, Wijk K. Seismic wave attenuation in carbonates. *J Geophys Res Solid Earth*. 2009;114(B6), B06208. https://doi.org/10.1029/2008JB005890.

28  Ba J, Zhao J, Carcione JM, Huang X. Compressional wave dispersion due to rock matrix stiffening by clay squirt flow: clay squirt flow in tight siltstone. *Geophys Res Lett*. 2016;43(12):6186–6195. https://doi.org/10.1002/2016GL069312.

29  Ba J, Xu W, Fu LY, Carcione JM, Zhang L. Rock anelasticity due to patchy saturation and fabric heterogeneity: a double double-porosity model of wave propagation. *J Geophys Res Solid Earth*. 2017;122(3):1949–1976. https://doi.org/10.1002/2016JB013882.

30  Ba J, Ma R, Carcione JM, Picotti S. Ultrasonic wave attenuation dependence on saturation in tight oil siltstones. *J Pet Sci Eng*. 2019;179:1114–1122. https://doi.org/10.1016/j.petrol.2019.04.099.

31  Borgomano JVM, Pimienta L, Fortin J, Guéguen Y. Dispersion and attenuation measurements of the elastic moduli of a dual-porosity limestone: elastic moduli dispersion in a limestone. *J Geophys Res Solid Earth*. 2017;122(4):2690–2711. https://doi.org/10.1002/2016JB013816.

32  Borgomano JVM, Pimienta LX, Fortin J, Guéguen Y. Seismic dispersion and attenuation in fluid-saturated carbonate rocks: effect of microstructure and pressure. *J Geophys Res Solid Earth*. 2019;124(12):12498–12522. https://doi.org/10.1029/2019JB018434.

33  Das V, Mukerji T, Mavko G. Scale effects of velocity dispersion and attenuation ($Q^{-1}$) in layered viscoelastic medium. *Geophysics*. 2019;84(3):T147–T166. https://doi.org/10.1190/geo2018-0154.1.

34  Ma R, Ba J. Coda and intrinsic attenuations from ultrasonic measurements in tight siltstones. *J Geophys Res Solid Earth*. 2020;125(4), e2019JB018825. https://doi.org/10.1029/2019JB018825.

35  Matsushima J, Suzuki M, Kato Y, Rokugawa S. Ultrasonic measurements of attenuation and velocity of compressional and shear waves in partially frozen unconsolidated sediment and synthetic porous rock. *Geophysics*. 2016;81(2):D141–D153. https://doi.org/10.1190/geo2015-0350.1.

36  Tompkins MJ, Christensen NI. Ultrasonic *P* - and *S* -wave attenuation in oceanic basalt. *Geophys J Int*. 2001;145(1):172–186. https://doi.org/10.1046/j.0956-540x.2001.01354.x.

37  Zhubayev A, Houben ME, Smeulders DMJ, Barnhoorn A. Ultrasonic velocity and attenuation anisotropy of shales, Whitby, United Kingdom. *Geophysics*. 2016;81(1):D45–D56. https://doi.org/10.1190/geo2015-0211.1.

38  Yurikov A, Lebedev M, Pervukhina M. Ultrasonic velocity measurements on thin rock samples: experiment and numerical modeling. *Geophysics*. 2018;83(2):MR47–MR56. https://doi.org/10.1190/geo2016-0685.1.

39  Toksöz MN, Johnston DH, Timur A. Attenuation of seismic waves in dry and saturated rocks: I. Laboratory measurements. *Geophysics*. 1979;44(4):681–690. https://doi.org/10.1190/1.1440969.

40  Quan Y, Harris JM. Seismic attenuation tomography using the frequency shift method. *Geophysics*. 1997;62(3):895–905. https://doi.org/10.1190/1.1444197.

41  Akram J, Eaton DW. A review and appraisal of arrival-time picking methods for downhole microseismic data. *Geophysics*. 2016;81(2):KS71–KS91. https://doi.org/10.1190/geo2014-0500.1.

42  Qi Q, Müller TM, Pervukhina M. Sonic QP/QS ratio as diagnostic tool for shale gas saturation. *Geophysics*. 2017;82(3):MR97–MR103. https://doi.org/10.1190/geo2016-0499.1.

43  Sun X, Tang X, Cheng CH (Arthur), Frazer LN. P- and S-wave attenuation logs from monopole sonic data. *Geophysics*. 2000;65(3):755–765. https://doi.org/10.1190/1.1444774.

44  Yang H, Duan HF, Zhu JB. Thermal effect on compressional wave propagation across fluid-filled rock joints. *Rock Mech Rock Eng*. 2021;54(1):455–462. https://doi.org/10.1007/s00603-020-02254-5.

45  Hu C, Tu N, Lu W. Seismic attenuation estimation using an improved frequency shift method. *Geosci Rem Sens Lett IEEE*. 2013;10(5):1026–1030. https://doi.org/10.1109/LGRS.2012.2227933.

46  Zhang C, Ulrych TJ. Estimation of quality factors from CMP records. *Geophysics*. 2002;67(5):1542–1547. https://doi.org/10.1190/1.1512799.

47  Giri A, Tarafdar S, Gouze P, Dutta T. Fractal geometry of sedimentary rocks: simulation in 3-D using a relaxed bidisperse ballistic deposition model. *Geophys J Int*. 2013;192(3):1059–1069. https://doi.org/10.1093/gji/ggs084.

48  Katz AJ, Thompson AH. Fractal sandstone pores: implications for conductivity and pore formation. *Phys Rev Lett*. 1985;54(12):1325–1328. https://doi.org/10.1103/PhysRevLett.54.1325.

49  Krohn CE. Fractal measurements of sandstones, shales, and carbonates. *J Geophys Res Solid Earth*. 1988;93(B4):3297–3305. https://doi.org/10.1029/JB093iB04p03297.

50  Yu B, Li J. Some fractal characters of porous media. *Fractals*. 2001:365–372. https://doi.org/10.1142/S0218348X01000804, 09(03.

51  Berryman JG. Single-scattering approximations for coefficients in Biot's equations of poroelasticity. *J Acoust Soc Am*. 1992;91(2):551–571. https://doi.org/10.1121/1.402518.

52  Ba J, Carcione JM, Nie JX. Biot-Rayleigh theory of wave propagation in double-porosity media. *J Geophys Res*. 2011;116(B6), B06202. https://doi.org/10.1029/2010JB008185.

53  Zhang L, Ba J, Carcione JM, Fu LY. Differential poroelasticity model for wave dissipation in self-similar rocks. *Int J Rock Mech Min Sci*. 2020;128, 104281. https://doi.org/10.1016/j.ijrmms.2020.104281.

54  Hashin Z, Shtrikman S. A variational approach to the theory of the elastic behaviour of multiphase materials. *J Mech Phys Solid*. 1963;11(2):127–140. https://doi.org/10.1016/0022-5096(63)90060-7.

55  Batzle M, Wang Z. Seismic properties of pore fluids. *Geophysics*. 1992;57(11):1396–1408. https://doi.org/10.1190/1.1443207.

56  Li P, Zheng M, Bi H, Wu S, Wang X. Pore throat structure and fractal characteristics of tight oil sandstone: a case study in the Ordos Basin, China. *J Pet Sci Eng*. 2017;149:665–674. https://doi.org/10.1016/j.petrol.2016.11.015.

57  Golsanami N, Fernando SG, Jayasuriya MN, et al. Fractal properties of various clay minerals obtained from SEM images. In: Liu Q, ed. *Geofluids*. 2021:1–18. https://doi.org/10.1155/2021/5516444, 2021.

58  Gurevich B, Makarynska D, de Paula OB, Pervukhina M. A simple model for squirt-flow dispersion and attenuation in fluid-saturated granular rocks. *Geophysics*. 2010;75(6):N109–N120. https://doi.org/10.1190/1.3509782.

59  Zhang L, Ba J, Carcione JM. Wave propagation in infinituple-porosity media. *J Geophys Res Solid Earth*. 2021;126(4). https://doi.org/10.1029/2020JB021266. e2020JB021266.

60  Zhang L, Ba J, Carcione JM, Wu C. Seismic wave propagation in partially saturated rocks with a fractal distribution of fluid-patch size. *J Geophys Res Solid Earth*. 2022;127(2). https://doi.org/10.1029/2021JB023809. e2021JB023809.